Available online at www.sciencedirect.com
SCIENCE DIRECT®
Journal of Power Sources 141 (2005) 47–64
JOURNAL OF POWER SOURCES
www.elsevier.com/locate/jpowsour

Analysis and design of PEM fuel cells

V. Mishra, F. Yang, R. Pitchumani*

Advanced Materials and Technologies Laboratory, Department of Mechanical Engineering, University of Connecticut, Storrs, CT 06269-3139, USA

Received 20 July 2004; received in revised form 29 August 2004; accepted 29 August 2004
Available online 5 November 2004

Abstract

This paper presents a detailed numerical investigation of the transport and electrochemical phenomena involved during the operation of a single proton exchange membrane (PEM) fuel cell on reformate feed with a view to developing optimal design and operating conditions. A one-dimensional non-isothermal model, validated with experimental data, is utilized to evaluate the fuel cell performance over a wide range of design and operating parameters that affect the thermal response and water management. Based on a systematic parametric analysis on the various physical and electrochemical phenomena, feasible operating regimes and optimal design conditions are identified with the objective of maximizing the power density subject to constraints. Overall, this paper illustrates a methodology for using physics-based models for cell design and optimization.

Keywords: PEM fuel cell; Mathematical model; CO poisoning; Cell optimization

1. Introduction

Proton exchange membrane (PEM) fuel cells are promising power-generation sources for mobile and stationary applications. In a typical PEM fuel cell, a polymer membrane is inserted between an anode and a cathode electrode to form a membrane electrode assembly (MEA), which is further sandwiched between two bipolar plates housing the flow channel, as shown in Fig. 1. A thin catalyst layer exists between each of electrodes and the membrane, referred to as the anode and cathode catalyst layer, respectively. The advantages of PEM fuel cells include the ability to provide high current densities at relatively low operating temperature and pressure, quick start-up, and pollution-free operation [1]. The high cost and low reliability of fuel cells, however, are the limiting factors for their widespread commercialization. A good understanding of the effects of the design and operating conditions on the voltage losses is required to reduce the capital cost and improve the reliability. Accordingly, two major groups of parameters may be identified, namely the operating parameters, e.g., temperature, pressure, reactant stoichiometry, and gas composition, and design parameters, e.g., thickness of cell components, electrode porosity, and platinum catalyst loading.

Water and thermal management are critical to the overall cell performance [2–7]. To maintain ionic conductivity, the membrane in a PEM fuel cell requires adequate humidification, which raises the critical issue of water management. During practical operation of fuel cells, both the gas streams are humidified to ensure the proper membrane hydration. However, excessive water will accumulate in the electrode pores and result in the electrode flooding, which degrades the cell performance by preventing the reactants from reaching the catalyst sites. In general, higher operating temperature is desirable due to decreased mass transport limitations and increased electrochemical reaction rates; at the same time, high temperatures may lead to increased mass transport losses due to the increase in water vapor pressure. A careful design of the cell and its operating parameters is therefore imperative to balance such competing constraints.

In the last decade, efforts on modeling and computer simulation of PEM fuel cells have been directed towards bet-

* Corresponding author. Tel.: +1 860 486 0683/2090; fax: +1 860 486 5088.
E-mail address: r.pitchumani@uconn.edu (R. Pitchumani).

0378-7753/$ – see front matter © 2004 Elsevier B.V. All rights reserved.
doi:10.1016/j.jpowsour.2004.08.051

Nomenclature

a	active reaction area per unit volume ($cm^2\ cm^{-3}$)
b_{fc0}	back-to-forward CO adsorption ratio (atm)
b_{fh}	back-to-forward H_2 adsorption ratio (atm)
c_i	molar concentration of species i ($mol\ cm^{-3}$)
$c_{p,i}$	specific heat at constant pressure for species i ($J\ mol^{-1}\ K^{-1}$)
D_i	diffusivity of species i in membrane ($cm^2\ s^{-1}$)
D_{ij}	diffusivity of species i in species j ($cm^2\ s^{-1}$)
e_e	electrode porosity
E_{cell}	cell potential difference (V)
F	Faradays constant, 96 487 ($C\ mol^{-1}$)
h_{vap}	enthalpy of vaporization ($J\ g^{-1}$)
i_m	catalyst layer membrane phase current density ($A\ cm^{-2}$)
i_s	catalyst layer solid-phase current density ($A\ cm^{-2}$)
i_0	exchange current density ($A\ cm^{-2}$)
I	operating current density ($A\ cm^{-2}$)
$j(X)$	total reaction rate ($A\ cm^{-3}$)
$j_i(X)$	reaction rate of species i ($A\ cm^{-3}$)
k_{fc}	electrode forward CO adsorption rate times $2F$ ($A\ cm^{-2}\ atm^{-1}$)
k_{fh}	electrode forward H_2 adsorption rate times $2F$ ($A\ cm^{-2}\ atm^{-1}$)
k_p	hydraulic permeability (cm^2)
L	characteristic length scale (cm)
m	catalyst loading ($g\ cm^{-2}$)
N_i	molar flux of species i ($mol\ cm^{-2}\ s^{-1}$)
p	pressure (atm)
p_a	anode pressure (atm)
R	universal gas constant 8.314 ($J\ mol^{-1}\ K^{-1}$)
ΔS	entropy change ($J\ g^{-1}\ K^{-1}$)
Sh	Sherwood number
t_{cl}	catalyst thickness (cm)
t_{el}	electrode thickness (cm)
t_{me}	membrane thickness (cm)
T	temperature (K)
W_i	molar mass of species i ($g\ mol^{-1}$)
x	position coordinate along the cell thickness
x_i	mole fraction of species i

Greek symbols

α_a	*apparent transfer coefficient for anodic reaction*
α_c	*apparent transfer coefficient for cathodic reaction*
δ	*membrane expansion coefficient*
η_d	*electro-osmotic drag coefficient*
κ	*thermal conductivity ($W\ cm^{-1}\ K^{-1}$)*
λ	*membrane hydration coefficient (moles of water per mole charge sites)*
μ	viscosity ($g\ cm^{-1}\ s^{-1}$)
ϕ_m	membrane phase potential (V)
ϕ_s	solid-phase potential (V)
σ	electronic conductivity ($\Omega^{-1}\ cm^{-1}$)
θ_1	hydrogen coverage
θ_4	CO coverage
ω_i	mass source for species i ($g\ cm^{-3}$)

Subscripts

an	*anode*
ca	*cathode*
cat	*catalyst*
el	*electrode*
g	*gas*
l	*liquid*
me	*membrane*
ref	*reference*

Superscripts

eff	*effective*
i	*boundary i*

ter understanding of the cell operation and performance. Bernardi and Verbrugge [8,9] and Springer et al. [10,11] studied the steady-state isothermal operation of PEM fuel cells using a one-dimensional model, and assuming perfect membrane hydration. Baschuk and Li [12] studied the effects of variant degree of water flooding in the cathode electrode/catalyst layer on the overall cell performance using a steady-state one-dimensional approach. Their study demonstrated that flooding has a significant impact on cell performance. Rowe and Li [13] performed a complete study on the water and thermal management on PEM fuel cells using a steady-state one-dimensional approach, and prescribed water vapor mole flux at the interfaces of electrodes and catalyst layers.

A two-dimensional model of transport phenomena in PEM fuel cells was presented by Gurau et al. [14], and the effects of oxygen and water vapor mole fraction distribution on the cell performance were illustrated. Um et al. [15] proposed a transient, single-phase two-dimensional model for electrochemical and transport processes in a PEM fuel cell. The heat management was neglected by assuming isothermal operation. Amphlett et al. [16,17] studied the transient response of a fuel cell stack by performing a global heat and mass balance analysis, while ignoring the details of electrochemical phenomena inside the cell. A two-dimensional isothermal model was developed by Wang et al. [18] to study the two-phase flow and transport in the cathode side. The liquid water formation and its effects on the reaction rate and species transport were analyzed. You and Liu [19] and You [20]

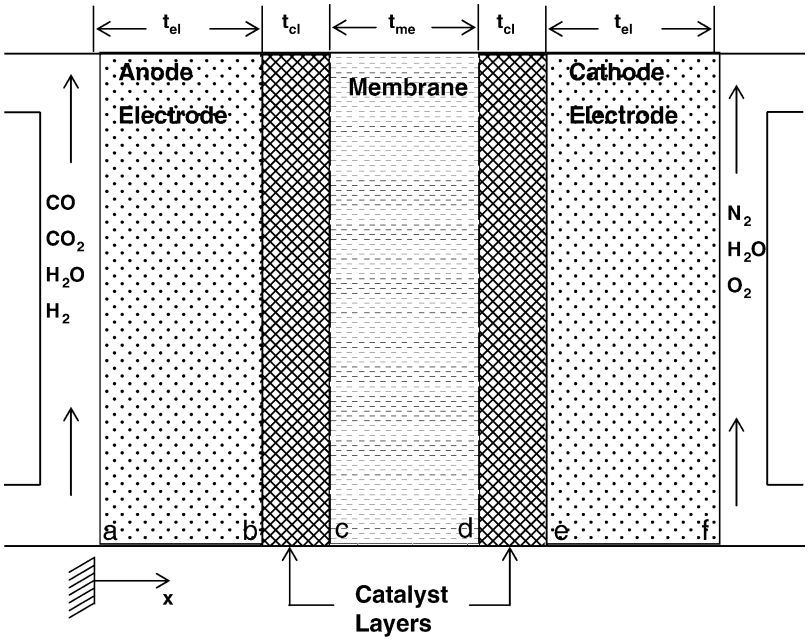

Fig. 1. Schematic illustration of a PEM fuel cell.

presented a two-dimensional steady-state isothermal model which couples the flow species, potential and current density distributions in an individual fuel cell. Although the two-phase flow was restricted to the cathode electrode, the study shows that the incorporation of two-phase flow in the model is essential.

While modeling of the individual transport and electrochemical phenomena has been reported collectively in the literature and provides insight on fuel cell operation, a systematic study to quantitatively determine the optimal conditions from physics-based models is lacking. In view of this, a methodology for model-based design and optimization is presented for the first time based on the systematic parametric studies and consideration of a few illustrative constraints on cell operation. The model adopted in the present study combines the transport model from Rowe and Li [13] and the CO poisoning kinetics from Springer et al. [21], as briefly presented in the next section. The numerical model, validated with the available experimental and numerical results in the literature, is used to conduct a parametric exploration in terms of the operating and design parameters. Based on the parametric studies and specified constraints on the maximum allowable temperature difference, maximum allowable cell voltage and minimum desirable membrane hydration, operating windows are identified on the current density as a function of the various parameters.

2. Mathematical model

To introduce the methodology for model-based design and optimization of a PEM fuel cell, a physical model for the transport and electrochemical phenomena is needed. In this section, the transport model from Rowe and Li [13] and the electrochemical kinetics model from Springer et al. [21] are combined to predict the performance of a PEM fuel cell operating on reformate feed. The model considers the five distinct regions between the flow channels, as shown schematically in Fig. 1. The cell is considered to be operating at steady state, and since the primary aim of the study is to present a methodology for design and optimization of cells using physics-based models, the discussion is limited to a one-dimensional modeling in the direction along the cell thickness. The modeling further includes the effects of carbon monoxide (CO) poisoning of the catalysts, as is prevalent in fuel cells operating on a reformate feed, but is often neglected in fuel cell modeling. The governing equations for the electrode, catalyst and membrane regions are presented in the following sections.

2.1. Electrodes

Fuel cell electrodes are typically made of porous carbon paper or cloth, which serves to transfer the reactant species and to conduct electrical current. The mathematical model is obtained by considering the conservation of the species, momentum and energy. Since the viscous force and pressure gradient are assumed to be zero in the electrode regions, the solution of the one-dimensional steady-state momentum equation yields constant velocity of the feeding gas mixtures. Following the development by Rowe and Li [13], the governing equations may be written as

$$\text{Species}: \quad \frac{\mathrm{d}N_i}{\mathrm{d}x} = \frac{\omega_i}{W_i} \tag{1}$$

$$\text{Energy}: \quad -k^{\text{eff}}\frac{\mathrm{d}^2T}{\mathrm{d}x^2} + \left[\sum_i N_i W_i c_{p,i} + N_{\text{l}} W_3 c_{p,\text{l}}\right] \times \frac{\mathrm{d}T}{\mathrm{d}x} + h_{\text{vap}}\omega_3 - \frac{I^2}{\sigma^{\text{eff}}} = 0 \tag{2}$$

where the subscript i denotes the ideal gas species i, N_i the molar flux in the x-direction in Fig. 1, ω_i the mass source term, W_i the molecular weight, k^{eff} the effective thermal conductivity, T the temperature, $c_{p,i}$ the specific heat at constant pressure, N_{l} the molar flux of liquid water, h_{vap} the enthalpy of vaporization for water, I the current density, σ^{eff} the effective electrical conductivity and the summation $\sum_i$ is performed with respect to all the gas species in the mixture.

In this study, the feed streams are considered to be reformate fuel at the anode side and humidified air at the cathode side. Hence, the gas species i are defined as $1 = O_2$, $2 = N_2$, $3 = H_2O(g)$ (i.e., water vapor) for the cathode electrode; and $1 = H_2$, $2 = CO_2$, $3 = H_2O(g)$ and $4 = CO$ for the anode electrode. Note that the inclusion of the CO species in the modeling forms the primary distinction of the present model relative to that reported by Rowe and Li [13]. Since no electrochemical reaction occurs in the electrode regions, the mass source term ω_i is nonzero only for the water vapor species $i = 3$. Evidently, Eq. (1) indicates that the molar flux for the species O_2, N_2, H_2, CO_2 and CO are constants. To solve the water vapor flux N_3, the mass source term ω_3 (corresponding to the vaporization/condensation of the water species) is determined in terms of the temperature and species concentration x_3, which, in turn, is determined by the Stefan–Maxwell equation [13]. Furthermore, the electrical potential in the electrode in the electrode solid, Φ_{s}, is calculated by the Ohm's law, and the unknowns in the electrode regions are T, N_3, x_3 and Φ_{s}.

2.2. Catalyst layers

Catalyst layers are considered to be a mixture of membrane, platinum catalyst (solid) and void space in this study. Electrochemical reactions in the catalyst regions are coupled with the transport of mass and energy, resulting in a potential gradient across the cell. The overall half-cell electrochemical reaction in the cathode catalyst layer may be written as [13]:

$$O_2 + 4H^+ + 4e^- \longrightarrow 2H_2O(l) \tag{3}$$

where the oxygen species and the electrons from the cathode electrode region react with the protons from the membrane region to form liquid water. For a PEM fuel cell operating on reformate feed at the anode, the electrochemical reactions in the anode catalyst layer involve the competing adsorption processes of CO and H_2, and are represented by the four processes expressed in the following equations [21]:

$$CO + M \leftrightarrow (M{-}CO) \tag{4}$$

$$H_2 + 2M \leftrightarrow 2(M{-}H) \tag{5}$$

$$2(M{-}H) \longrightarrow 2H^+ + 2e^- + 2M \tag{6}$$

$$H_2O + (M{-}CO) \longrightarrow M + CO_2 + 2H^+ + 2e^- \tag{7}$$

The bidirectional arrow in Eq. (4) indicates that a free carbon monoxide molecule may be adsorbed to a vacant catalyst site, M, to form a CO molecule in the adsorbed state, (M–CO); in a reverse process, the adsorbed CO molecule may be desorbed to yield a free CO and a vacant site. Similarly, a hydrogen molecule may experience a reversible chemisorption process with two vacant catalyst sites to form two adsorbed hydrogen atoms. The two processes in Eqs. (6) and (7) generate the current corresponding to the electrochemical oxidation of the adsorbed hydrogen atoms and carbon monoxide molecule, respectively. Clearly, the CO and H_2 molecules compete with each other for the vacant catalyst sites, and high concentration of CO in the fuel may prevent the adsorption of the hydrogen molecules, leading to the so-called CO poisoning effect.

In this section, the subscript notation for the species involved in the anode catalyst layer is $1 = H_2$, $2 = H^+$, $3 = H_2O(l)$, $4 = CO$, $5 = CO_2$, and that for the cathode catalyst layer is $1 = O_2$, $2 = H^+$, $3 = H_2O(l)$. The governing equations for the various electrochemical and transport processes are derived by the application of conservation laws for the species and energy, along with the Bulter–Volmer equation for the electrochemical reactions, the Nernst–Planck equation for the flux of aqueous species in the membrane, and the Ohm's law for electron transfer in the solid.

2.2.1. Anode catalyst layer

The conservation equations of species and energy in the anode catalyst layer account for the electrochemical reactions of CO and H_2 as follows:

$$\text{Species } H_2: \quad \frac{\mathrm{d}N_1}{\mathrm{d}x} = -\frac{j_1(x)}{2F} \tag{8}$$

$$\text{Species } H^+: \quad F\frac{\mathrm{d}N_2}{\mathrm{d}x} = \frac{\mathrm{d}i_{\text{m}}}{\mathrm{d}x} = j_1(x) + j_4(x) \tag{9}$$

$$\text{Species } H_2O(l): \quad \frac{\mathrm{d}N_3}{\mathrm{d}x} = -\frac{j_4(x)}{2F} \tag{10}$$

$$\text{Species CO}: \quad \frac{\mathrm{d}N_4}{\mathrm{d}x} = -\frac{j_4(x)}{2F} \tag{11}$$

$$\text{Species } CO_2: \quad \frac{\mathrm{d}N_5}{\mathrm{d}x} = \frac{j_4(x)}{2F} \tag{12}$$

$$\text{Energy}: \quad -k^{\text{eff}}\frac{\mathrm{d}^2T}{\mathrm{d}x^2} + \left(\sum_{i=1,3-5} N_i c_{p,i} W_i\right) \times \frac{\mathrm{d}T}{\mathrm{d}x} + \left|\frac{j_1 + j_4}{2F}\right| (T\,\Delta S) = (j_1 + j_4)(\Phi_{\text{s}} - \Phi_{\text{m}}) + \frac{i_{\text{m}}^2}{\kappa^{\text{eff}}} \tag{13}$$

where the reaction rates $j_1(x)$ and $j_4(x)$ for H_2 and CO, respectively, may be given by the Butler–Volmer equation as

$$j_1(x) = ai_0^{\text{ref}}\theta_1\frac{c_1}{c_1^{\text{ref}}}\left[\exp\left(\frac{\alpha_a F}{RT}(\Phi_s-\Phi_m)\right) - \exp\left(\frac{-\alpha_c F}{RT}(\Phi_s-\Phi_m)\right)\right] \quad (14)$$

$$j_4(x) = ai_0^{\text{ref}}\theta_4\frac{c_4}{c_4^{\text{ref}}}\left[\exp\left(\frac{\alpha_a F}{RT}(\Phi_s-\Phi_m)\right) - \exp\left(\frac{-\alpha_c F}{RT}(\Phi_s-\Phi_m)\right)\right] \quad (15)$$

The parameter i_m is the catalyst layer membrane phase current density, which is related to the proton molar flux, N_2, via the Faraday constant, F, as $i_m = FN_2$. In the energy equation, Eq. (13), ΔS is the entropy change for the cathode reaction, Φ_s and Φ_m are the electrical potential in the catalyst solid phase and catalyst membrane phase, respectively, and κ^{eff} is the effective electrical conductivity of the membrane. The reaction rates, $j_1(x)$ and $j_4(x)$, depend on the catalyst reactive surface area per unit volume, a, the reference exchange current density, i_0^{ref}, at the reference oxygen concentration, c_1^{ref}, the fuel concentrations, c_1 and c_4, and the transfer coefficients α_a and α_c. Depending on the characteristics of the half-cell reactions and the material properties of the catalyst layers, the transfer coefficients, α_a and α_c, take on distinct values, each in a range between 0 and 1. Following Rowe and Li [13], both transfer coefficients are taken to be unity in this study, which yields an approximate Tafel slope of 70 mV decade^{-1}.

Since both CO and H_2 are oxidized to produce H^+, the species equation for proton flux, Eq. (9), includes the sum of $j_1(x)$ and $j_4(x)$. The species consumption/generation in the electrochemical reaction of carbon monoxide is represented by Eqs. (10)–(12). In the energy equation, Eq. (13), the summation $\sum$ includes four non-ionic species, and the sum $j_1(x) + j_2(x)$ is also introduced for the overall anode electrochemical reaction involving H_2 and CO. Note that the reaction rate $j_1(x)$ is proportional to the coverage of hydrogen molecules, θ_1, which is defined as the fraction of the catalyst reactive surface area covered by the adsorbed hydrogen. Similarly, the reaction rate of the CO species is considered to be proportional to the CO coverage, θ_4, and CO concentration c_4 in Eq. (15). Considering the adsorption, desorption and reaction processes in Eqs. (4)–(7), the coverage θ_1 and θ_4 may be obtained from a kinetic analysis for mass balance [21]:

$$k_{fc}x_4 p(1-\theta_4-\theta_1) - b_{fc}k_{fc}\theta_4 - j_4 = 0 \quad (16)$$

$$k_{fh}x_1 p(1-\theta_4-\theta_1)^2 - b_{fh}k_{fh}\theta_1^2 - j_1 = 0 \quad (17)$$

where the CO adsorption-to-desorption ratio, b_{fc}, is a function of the free energy variation, $\delta(\Delta G_{CO})$, for the CO adsorption/desorption process, and H_2 adsorption rate, k_{fh}, depends on the change in activation energy, $\delta(\Delta E_H)$, for hydrogen dissociative adsorption near CO-occupied catalyst site. Since the species H_2 and CO exhibit different adsorption/desorption kinetics, with the CO following a more complex Temkin kinetics, the values of $\delta(\Delta G_{CO})$ and $\delta(\Delta E_H)$ are different, as seen in Table 1 [21].

Table 1
Kinetic parameters for the electrochemical reactions of CO

b_{fc0} (atm)	1.5×10^{-8}
b_{fh} (atm)	0.5
k_{ec} (A cm^{-2})	1×10^{-8}
k_{eh} (A cm^{-2})	4.0
k_{fc} (A cm^{-2} atm^{-1})	10
k_{fh} (A cm^{-2} atm^{-1})	4000
$\delta(\Delta G_{CO})/RT$	7.8
$\delta(\Delta E_H)/RT$	4.6

The six conservation equations for the anode catalyst layer, Eqs. (8)–(13), introduce four additional unknowns, namely c_1, c_4, Φ_s and Φ_m, which, in turn, are determined by the Nernst–Planck equation and Ohm's law [13]. Note that 10 unknowns are involved in the anode catalyst region: N_1, i_m, N_3, N_4, N_5, T, c_1, c_4, Φ_m and Φ_s. The governing equations for the cathode catalyst layer follow those given by Rowe and Li [13], and are not repeated here for brevity.

2.3. Membrane

The membrane of a PEM fuel cell is generally made of a perflourosulfonate polymer, which acts as a proton conductor when saturated with water. Based on the model assumptions, only two species are present in the membrane region, i.e., the liquid water and the proton. Since no chemical reaction takes place in the membrane, the species conservation indicates constant fluxes for both species. The flux of water is determined by the net effect of electro-osmotic drag, diffusion due to concentration gradient and convection due to pressure gradient. The flux of protons is described by the Nernst–Planck equation, which is further rearranged to be in the form of the membrane potential in this study. The conservation equations of energy and species in the membrane region read [13]:

$$\text{Energy}: \quad -k^{\text{eff}}\frac{d^2T}{dx^2} + \frac{d}{dx}(N_l h_l W_l) = \frac{i_m^2}{\kappa} \quad (18)$$

$$\text{Potential}: \quad \frac{d\Phi_m}{dx} = -\frac{i_m}{\kappa} + \delta\frac{RT}{F}\left(\frac{3}{1+\delta\lambda}\right)\frac{d\lambda}{dx} + \frac{F}{\kappa}\left(\frac{1}{\lambda}\right)N_l \quad (19)$$

$$H_2O\ \text{flux}: \quad N_l = -D_l\frac{dc_l}{dx} - \epsilon_w^{\text{mem}}c_l\frac{k_p}{\mu}\left(\frac{dp}{dx}\right) + \frac{\eta_d I}{F} \quad (20)$$

where the subscript l denotes the liquid water species, h the specific enthalpy, κ the proton conductivity of the membrane, δ the membrane expansion coefficient, λ the membrane hy-

dration, D_l the diffusion coefficient for liquid water in the membrane, ϵ_w^{mem} the volume fraction of water in the membrane, k_p the hydraulic permeability of the membrane, μ the viscosity of liquid water and η_d the electro-osmotic drag coefficient. Eqs. (18)–(20) are solved for the three unknowns: T, Φ_m and N_l, and the readers are referred to Rowe and Li [13] for the values of various physical properties involved.

The governing equations formulated in Sections 2.1–2.3 are solved with the following boundary conditions specified at the inlets of the anode and cathode electrodes (i.e., at the points a and f in Fig. 1): temperature, composition of the reactant gas mixtures, pressure and flow rate in terms of stoichiometry. It must be pointed out that the water vapor flux, N_3, could be calculated by considering the condensation/vaporization processes in the porous electrode regions. However, due to the difficulty in solving two-phase flow in the porous media, the values of N_3 at the electrode/catalyst interfaces, i.e., points b and e, are set to be 10% of the corresponding flux of the reactant mixture, as suggested by Rowe and Li [13] for convenience. An algorithm developed by Fan and White [22] was implemented to predict the polarization curve, temperature distribution, species concentration and flux under various operating conditions. The physical properties and kinetic data adopted in the simulations are available in Refs. [13,21].

3. Results and discussion

The validation of the current model is first examined through comparison with numerical and experimental results in the literature. Using the parameter combination for the base case listed in Table 2, the predicted polarization curve is compared to the numerical results from Rowe and Li [13] in Fig. 2 for the case of pure hydrogen at 3 atm as fuel. In the figure, the line corresponds to the present simulation results, while the discrete circle markers denote numerical prediction by Rowe and Li. The results of the model in this paper are seen to be in good agreement with those of Rowe and Li for the range of current density considered. The cell potential decreases monotonically with increasing current density, owing to increased ohmic loss in the membrane, and activation and concentration losses in the catalyst regions. When the current density increases to around 1.0 A cm^{-2}, the concentration polarization becomes dominant due to the limitation of mass transport rate. The partial pressure of oxygen at the catalyst layer/cathode interface approaches zero when $I = 1.1$ A cm^{-2}, which is taken as the limiting current density for this case.

Fig. 2 also compares the polarization curve prediction with experimental data from Springer et al. [21] for a PEM fuel cell operated on reformate feed with three CO concentrations. In addition to Table 2, the kinetic parameters used in the calculation for the electrochemical reactions of CO are given in Table 1. Again, good agreement is observed between the model simulations and the experimental measurements.

Table 2
Base case model parameters

Cell temperature, T_c (K)	353.0
Anode pressure, p_a (atm)	3.0
Cathode pressure, p_c (atm)	3.0
Anode stoichiometry, ζ_a	1.5
Cathode stoichiometry, ζ_c	3.0
Relative humidity, RH	100
Electrode thickness, t_{el} (μm)	200
Catalyst layer thickness, t_{cl} (μm)	7
Membrane thickness, t_{me} (μm)	180
Volume fraction of membrane in catalyst layer, e_m^{cl}	0.45
Volume fraction of solid in catalyst layer, e_s^{cl}	0.5
Anode dry gas mole fraction (CO_2/H_2)	0.0
Cathode dry gas mole fraction (N_2/O_2)	3.76
Reversible potential, E_{oc} (V)	1.199
Anode: ai_0^{ref} (A cm^{-3})	30000
Cathode: ai_0^{ref} (A cm^{-3})	0.0095
Thermal conductivity electrode, k_{el} (W cm^{-1} K^{-1})	0.026
Thermal conductivity of dry membrane, k_{me} (W cm^{-1} K^{-1})	0.00673
Thermal conductivity of water, k_w (W cm^{-1} K^{-1})	0.0024
$(Sh\ f_e)$/L (cm^{-2})	20000

Recall that the CO species is adsorbed on the catalyst surface, blocking the electrochemical reaction of the hydrogen fuel. Consequently, smaller cell potential is seen for a fixed value of current density when CO concentration increases from 0 to 250 ppm in Fig. 2. The limiting current density for the three cases with CO poisoning effects reduces to around 0.6 A cm^{-2}, due to the high coverage of CO species and low partial pressure of the hydrogen at the catalyst layer/anode interface. Note that a sharp drop of E_{cell} is observed between $I = 0.2$ and 0.4A cm^{-2} for the case of 100 ppm CO concentration. For the highest CO concentration considered in this study, i.e., 250 ppm, significant loss of E_{cell} is observed as $I > 0.1$. Overall, the model predictions show good agreement with the numerical and experimental results in the literature. This forms a reliable basis for the use of the numerical model

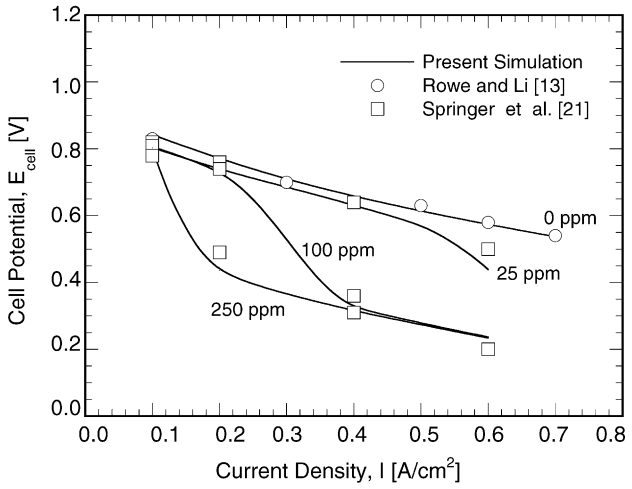

Fig. 2. Validation of the present model with numerical result of Rowe and Li [13] and experimental data of Springer et al. [21] for the CO concentrations identified.

in conducting the parametric studies discussed in the remainder of this section.

For better understanding of the transport and electrochemical processes involved, it is illustrative to first examine the distributions of the species concentration and flux, temperature and potential across the fuel cell thickness. To this end, Figs. 3 and 4 present the variables of interest as functions of the location x within the cell at three current densities. The values of the parameters adopted in Fig. 3 are listed in Table 2. Fig. 3(a) shows the influence of current density on the concentration distribution of the species H_2 and O_2. For the case considered, the species in the anode electrode are the hydrogen and water vapor, which corresponds to a relatively large value of diffusivity for H_2 [13]. Thus, the Stefan–Maxwell equation indicates that a small concentration gradient of H_2 is needed in the porous anode to maintain the hydrogen flux to the anode catalyst layer. However, the mutual diffusivities of the oxygen in the humidified air mixture are small, leading to relatively large c_{O_2} gradient in the cathode, as seen in Fig. 3(a). Note that the positive gradient of c_{O_2} corresponds to the oxygen flux from the cathode electrode to the cathode catalyst layer. Increase in the current density calls for the increase in the feed stream fluxes, which, in turn, is responsible for the increase in the gradients of c_{O_2} and c_{H_2} in the electrodes by virtue of the Stefan–Maxwell equation. Due to the electrochemical reactions, the concentrations of both reactants drop to zero in the catalyst layers. Since the reactions occur only in the inlet portion of the catalyst layers in this case, the thickness of both catalyst layers may be reduced to save the precious catalyst metal.

The distribution of water vapor concentration in terms of relative humidity (RH) is presented in Fig. 3(b).

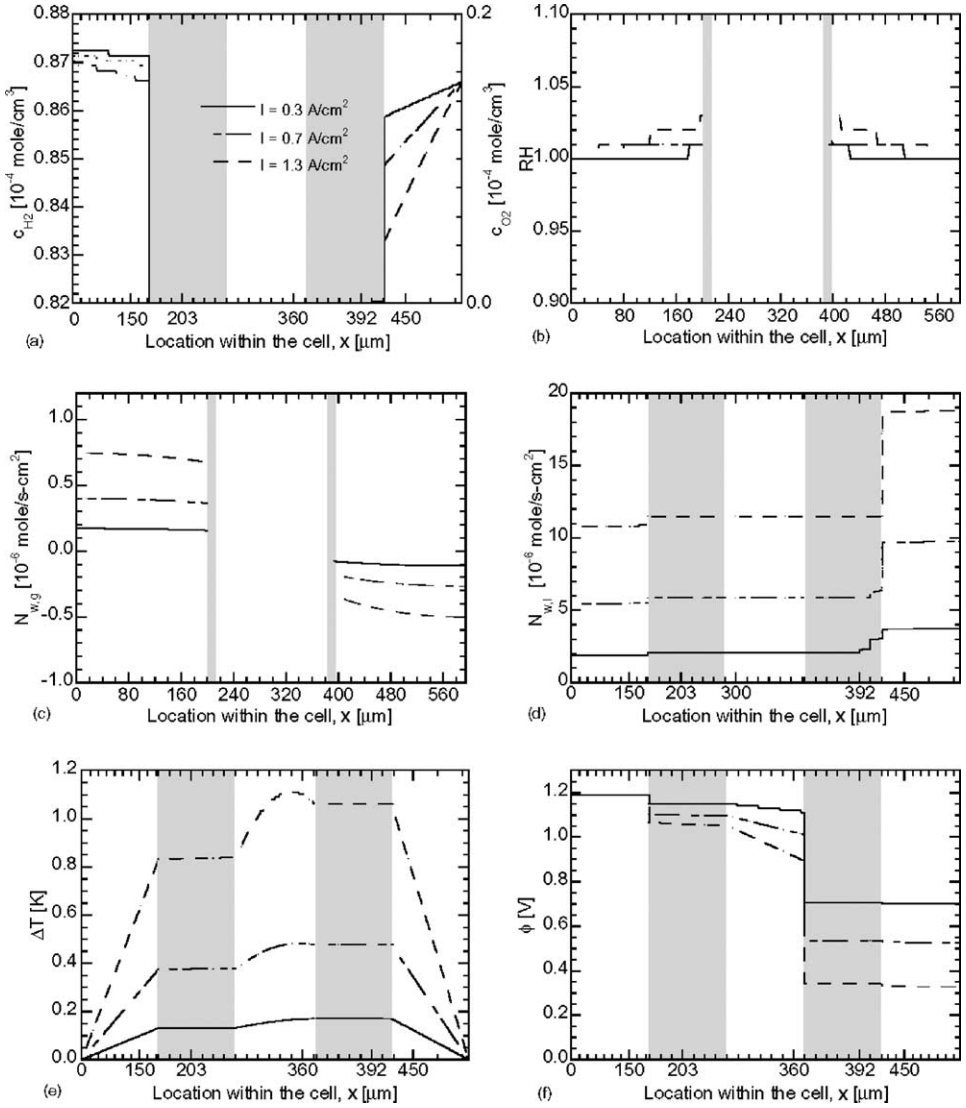

Fig. 3. Profiles of (a) hydrogen and oxygen concentrations, c_{H_2} and c_{O_2}, (b) relative humidity, RH, (c) water vapor flux, $N_{w,g}$, (d) liquid water flux, $N_{w,l}$, (e) temperature difference, ΔT and (f) potential, ϕ, across the cell thickness at three current densities. The shaded regions denote the catalyst layers, and the results correspond to the parameter combination given in Table 2.

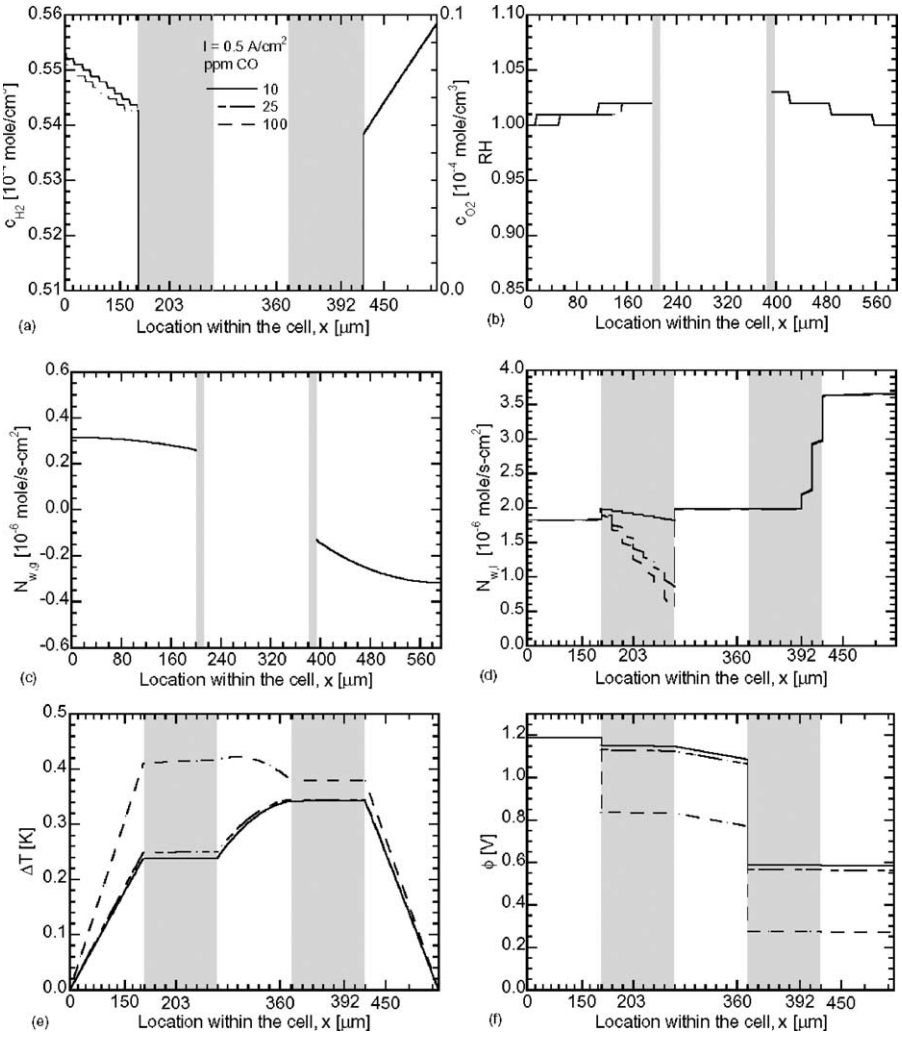

Fig. 4. Profiles of (a) hydrogen and oxygen concentrations, c_{H_2} and c_{O_2}, (b) relative humidity, RH, (c) water vapor flux, $N_{w,g}$, (d) liquid water flux, $N_{w,l}$, (e) temperature difference, ΔT and (f) potential, ϕ, across the cell thickness at three current densities. The shaded regions denote the catalyst layers, and the results correspond to $p_a = 1$ atm, and the other parameters are given in Tables 1 and 2.

Recall that the total pressure in the electrodes is assumed to be constant; therefore, the concentration of the water vapor increases towards the catalyst layer/electrode interfaces to balance the corresponding decreases in reactant concentrations in Fig. 3(a). For higher current density, the water vapor concentration near the catalyst layer/electrode interfaces becomes higher, which is instrumental for membrane hydration. The values of relative humidity are greater than 1 in Fig. 3(b), indicating that water condensation occurs in both electrode regions.

Fig. 3(c) and (d) shows the flux distribution of water vapor and liquid water, respectively, across the cell. Because of the above-mentioned condensation process, $N_{w,g}$ ($N_{w,l}$) decreases (increases) monotonically with x in the electrode regions. Note that water vapor is present only in the electrode regions, while liquid water exists throughout the cell. In the membrane region, an increase in current density leads to increase in osmotic drag, which, in turn, results in increase in the liquid water flux. Rapid increase of the liquid water flux with increasing x is observed in the cathode catalyst layer, owing to the electrochemical reaction that generates liquid water in the region. Since the water fluxes are assumed to be proportional to the corresponding reactant mixture flux [13], both $N_{w,g}$ and $N_{w,l}$ increase with increasing current density in the electrode regions. The same assumption is responsible for the discontinuity of $N_{w,l}$ at the interface of catalyst layer/anode electrode, and a more accurate model accounting for the two-phase flow in the porous media needs to be incorporated in a future work.

The temperature profiles, $T - T_c$, across the entire cell are shown in Fig. 3(e) for the base case conditions given in Table 2. Linear variations are observed in the anode and cathode electrodes, indicating that heat transport in the region is predominantly through conduction with negligible heat generation from resistive heating. It is seen that a small temperature rise (<0.2 K) is achieved when $I = 0.3\,\mathrm{A\,cm^{-2}}$. With increasing current density, relatively larger temperature rise (about 1.1 K for the case of $I = 1.3\,\mathrm{A\,cm^{-2}}$) and

highly nonlinear profiles are observed in the membrane region, owing to the Joule heating from the ionic current. Since multiple cells are stacked together in typical application, the seemingly small temperature rise within a single cell and the temperature jump across the cell interface caused by contact resistance may accumulate, thereby causing a problem of thermal management.

Fig. 3(f) shows the electrical potential profiles along the cell thickness. A value of 1.19 V is set as the reference potential at the inlet of the anode electrode, i.e., point a in Fig. 1. The overpotential in the electrodes is negligible, owing to the high electrical conductivity of the electrode material. Significant activation loss and ohmic loss are seen in the catalyst layers and the membrane region, respectively. It must be mentioned that the anode activation loss is much larger compared to the results in the literature (e.g., [21]), which may be caused by a relatively slow hydrogen electrochemical reaction rate adopted in this study. Note that uncertainties exist for the value of the reaction rates since the value of some model parameters (e.g. c_1^{ref} in Eq. (14)) are not well documented in the literature. Furthermore, the polarizations increase with increasing current density, resulting in lower cell voltage as shown in Fig. 2(a)–(d).

Following the presentation format in Fig. 3, Fig. 4(a)–(f) illustrates the effects of CO concentration on the distribution of the variables of interest at a current density $I = 0.5\,\text{A cm}^{-2}$, and the parameter combination given in Tables 2 and 1. As seen previously in Fig. 3(a), the concentration gradient of H_2 in the anode electrode in Fig. 4(a) is smaller than that of O_2, due to the larger diffusivity of H_2 in the anode gas mixture. A small decrease of c_{H_2} in the anode electrode is observed with increasing CO concentration since the total pressure remains constant, while c_{O_2} on the cathode side is independent of the CO concentration on the anode side. In Fig. 4(b), the relative humidity in the anode electrode shows small decrease with increasing CO concentration, which may be explained by the reduction of water vapor diffusivity due to the presence of the CO species. Again, the CO concentration in the anode electrode exerts no influence on the relative humidity in the cathode electrode.

The water vapor flux profile in Fig. 4(c) remains fixed with respect to CO concentration, owing to the previously mentioned assumption that the water vapor flux is proportional to the flux of the reactant mixture (or current density). Fig. 4(d) shows that liquid water flux is independent of the CO concentration, except in the anode catalyst region. A decrease in liquid water flux in the anode catalyst region is observed with increasing CO concentration, which is due to the increased consumption of liquid water during the electrochemical reaction denoted by Eq. 7. Since higher CO concentration leads to larger concentration and activation losses in the catalyst region, the temperature profile in Fig. 4(e) shows larger temperature difference with increasing ppm CO. When the CO concentration increases from 10 to 25 ppm, slight increase of $T - T_c$ is seen, while relatively large increase of $T - T_c$ occurs as ppm CO increases further to 100. In Fig. 4(f), the overpotential in the anode catalyst region is seen to increase with the increase in CO concentration, and large voltage loss is observed when ppm CO equal to 100. Note that the ohmic loss in the membrane is invariant with respect to the CO concentration.

With the overview of the transport and electrochemical processes illustrated in Figs. 3 and 4, the model is further used in a parametric study to evaluate the performance of the fuel cell over a wide range of design and operation conditions. In this study, four quantities, namely the cell potential, E_{cell}, the power density, P, the maximum temperature rise, $\Delta T_{\max}$, and the minimum hydration $\lambda_{\min}$ are adopted to evaluate the overall fuel cell performance. It must be mentioned that the minimum hydration, $\lambda_{\min}$, is determined by the water vapor activity at the membrane/anode catalyst interface [13]. Systematic parametric runs are performed to calculate the four performance quantities as functions of the parameters involved in the model, and relevant results that are instrumental to design and operating optimization are presented in the remainder of this section. The parameters selected in the presentation are classified into two categories: (I) the operating parameters—current density, I, CO concentration in ppm, cell temperature, T_c, anode pressure, p_a, and relative humidity at anode, RH_a and (II) the design parameters—platinum loading, $m_{c,pt}$, membrane thickness, t_{me}, and porosity of the electrodes, e_e. The range of values of the operating and design parameters in the parametric study are chosen based on those commonly used in the literature [1,8,9,13,21]. The results from the parametric study are used for developing operating and design windows based on the maximization of the power density subject to practical constraints.

Fig. 5(a)–(d) presents the performance quantities as functions of the current density, I, for different values of CO concentration. In Fig. 5(a), the cell potential, E_{cell}, decreases monotonically with increasing I for fixed ppm CO and with increasing ppm CO for fixed current density, as previously seen in Fig. 2. When the ppm CO $\geq$ 50, the limiting current density is observed to be reduced to around $0.6\,\text{A cm}^{-2}$, and the corresponding cell potential reduces to a low value of 0.2 V. Fig. 5(b) shows the power density, P, as a function of the current density, I, and ppm CO. Since the power density P is defined as the product of the cell potential and current density, P initially increases with increasing I, for fixed CO concentration in Fig. 5(b). With further increase in the current density, the power density may decrease due to smaller cell potential, leading to the formation of peaks for the cases of ppm CO $\leq$ 50. When ppm CO $\geq$ 100, the drop of the cell potential is not significant in the vicinity of the limiting current density, and no power density peak is observed. For a fixed value of current density, P decreases monotonically with increasing CO concentration, owing to smaller cell potential caused by the CO poisoning effect.

The maximum temperature difference in the cell, $\Delta T_{\max}$, and the minimum hydration in the membrane, $\lambda_{\min}$, are shown as functions of I and CO ppm in Fig. 5(c) and (d), respectively. The maximum temperature difference is seen to in-

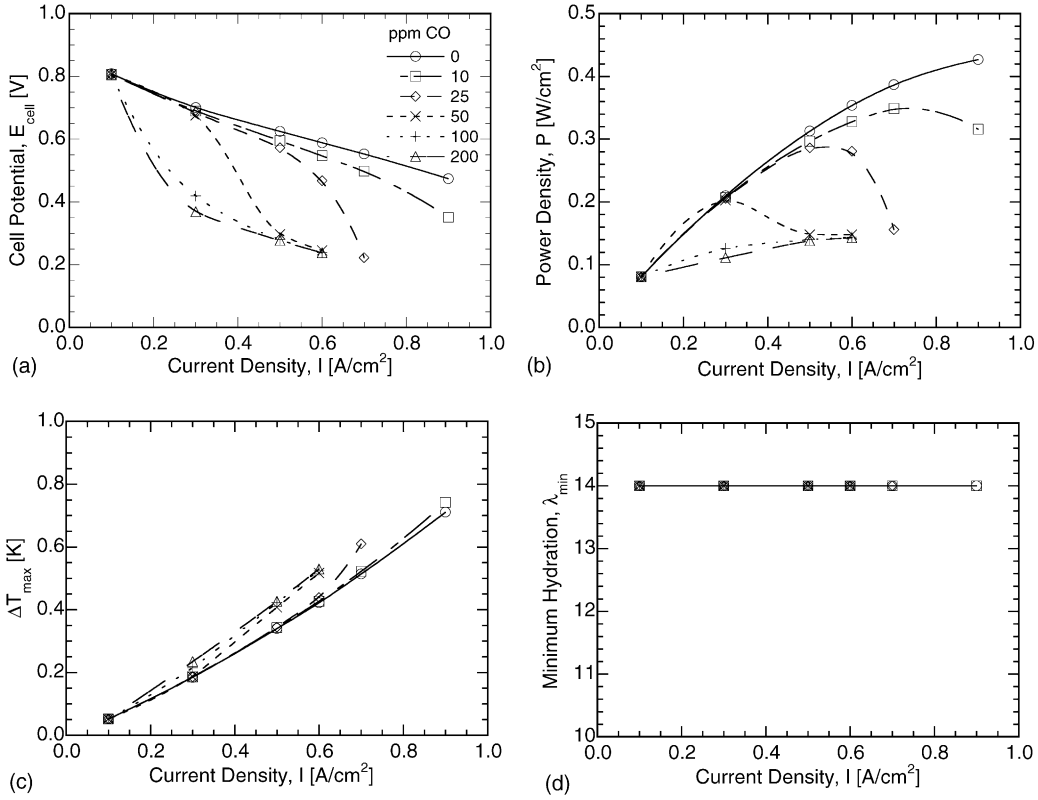

Fig. 5. Parametric effects of I and ppm CO on (a) cell potential, (b) power density, (c) maximum temperature difference and (d) minimum hydration. The default values of the other parameters are given in Tables 1 and 2.

crease monotonically with increasing current density, owing to more Joule heating in the membrane region at larger I. For fixed value of current density, the increase in CO concentration leads to higher overpotential in the catalyst region, which, in turn, is responsible for the increase in ΔT_{max}. Since the membrane hydration depends primarily on the concentration of the water species, λ_{min} is seen to remain a constant value of 14 for the range of current density and CO concentration considered in Fig. 5(d). The membrane material is in a well-hydrated state with high ionic conductivity as $\lambda_{min} \geq 14$.

Following the presentation format in Fig. 5, Figs. 6–8 illustrate the effects of the other operating parameters on the performance quantities. In Fig. 6(a), a range of operating temperature, T_c, between 293 and 363 K is chosen for typical PEM fuel cell operation. For fixed value of T_c, the cell potential E_{cell} decreases monotonically with increasing current density, as seen previously in Figs. 2–5. The cell potential increases when the operating temperature increases from 293 to 353 K, which may be explained by the reduced losses in the cell. The ionic conductivity increases with increasing temperature, leading to smaller resistive loss in the membrane. The transport losses are also reduced since the diffusivities increases with increasing T_c. Furthermore, the activation loss in the catalyst layer is smaller at higher operating temperatures [13]. However, further increase in operating temperature may cause increased partial water vapor pressure, leading to enhanced mass transport losses. Consequently, the cell voltage is seen to slightly decrease as T_c increases to 363 K.

Fig. 6(b) presents the power density, P, as a function of the current density, I, and the operating temperature, T_c. The effect of the operating temperature on the power density is similar to that on the cell potential, i.e., P increases initially with increasing T_c, and starts to decrease when $T = 363$ K. The maximum temperature difference in Fig. 6(c) decreases as T_c increases from 293 to 353 K, owing to the decreased losses mentioned above; a slight increase in ΔT_{max} is caused by the increased transport losses when $T_c = 363$ K. The minimum hydration in the membrane, λ_{min}, is shown as a function of I for different values of T_c in Fig. 6(d). For fixed value of T_c, λ_{min} is seen to decrease monotonically with increasing I, which may be attributed to the loss of the water species at the anode catalyst/membrane interface caused by the increased osmotic drag effect. The decrease in λ_{min} is more pronounced at lower temperatures, since water species cannot be effectively transferred to the membrane due to reduced diffusivities with temperature. The minimum hydration is seen to increase monotonically with the operating temperature for fixed values of I, owing to increased water vapor pressure at higher temperatures.

The effects of the anode pressure on the performance quantities are shown in Fig. 7(a)–(d). A non-monotonic trend is again observed in Fig. 7(a) for the relation between the cell potential, E_{cell}, and the anode pressure, p_a. When p_a

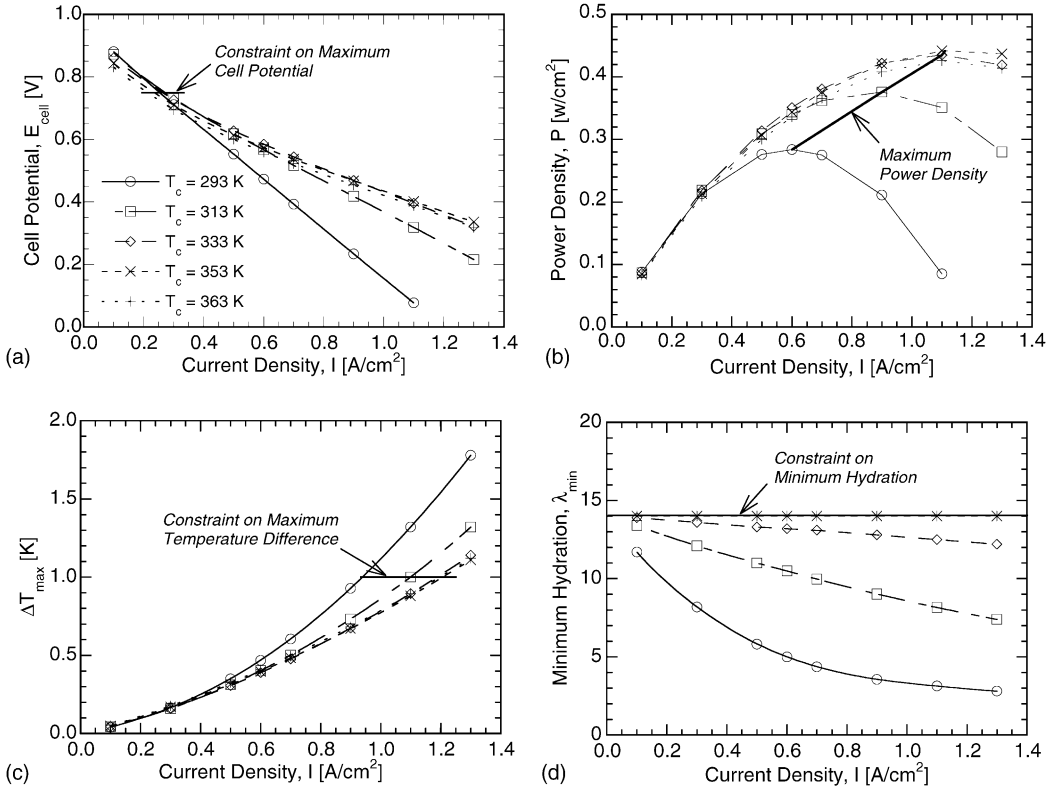

Fig. 6. Parametric effects of I and T_c on (a) cell potential, (b) power density, (c) maximum temperature difference and (d) minimum hydration. The default values of the other parameters are given in Tables 1 and 2.

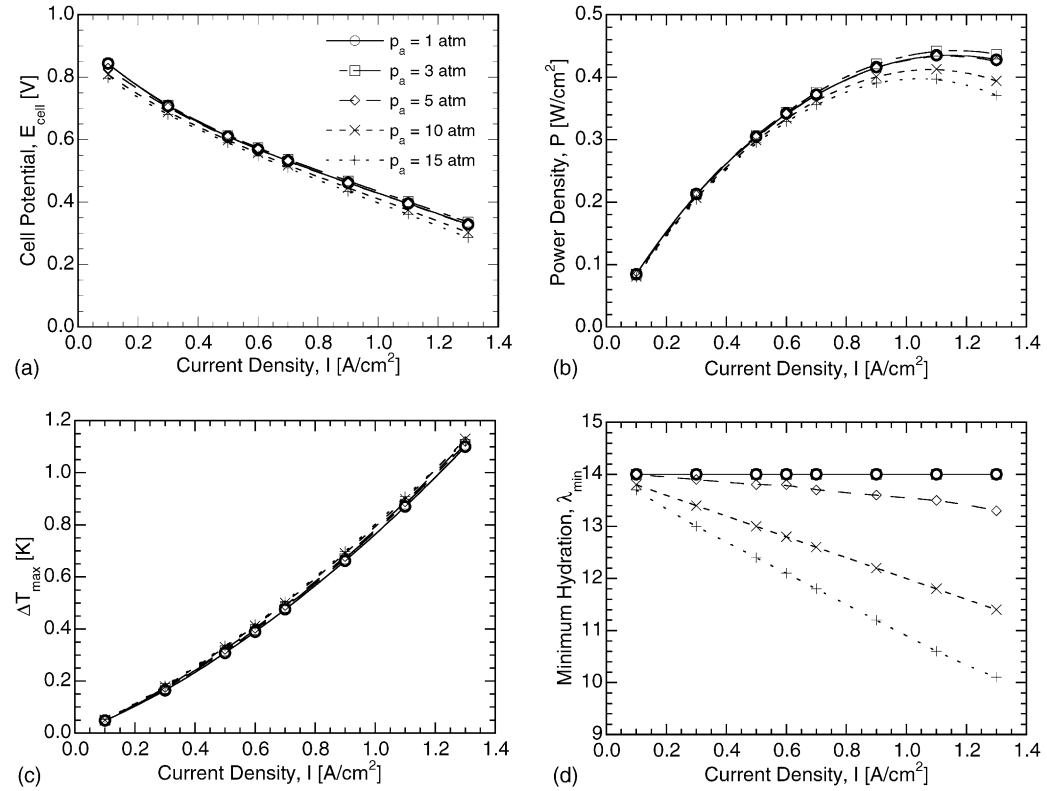

Fig. 7. Parametric effects of I and p_a on (a) cell potential, (b) power density, (c) maximum temperature difference and (d) minimum hydration. The default values of the other parameters are given in Tables 1 and 2.

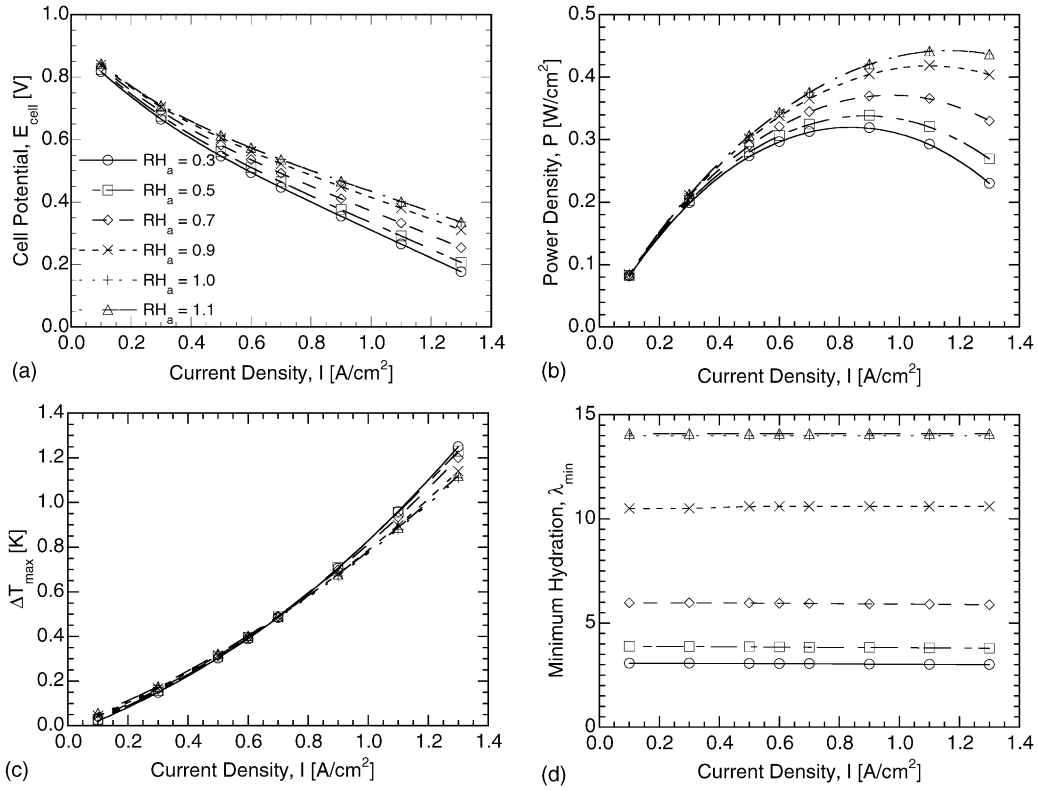

Fig. 8. Parametric effects of I and RH_a on (a) cell potential, (b) power density, (c) maximum temperature difference and (d) minimum hydration. The default values of the other parameters are given in Tables 1 and 2.

increases from 1 to 3 atm, higher partial pressure (or concentration) of hydrogen is present at the anode catalyst layer, leading to reduced concentration loss or higher cell potential. Further increase in p_a results in reduced water vapor diffusivity, which causes lower membrane hydration. The higher ohmic loss in the membrane, in turn, contributes to the lower cell potential. Overall, the influence of p_a on the cell potential is not as significant as that of the operating temperature in Fig. 6(a), for the range of parameters considered in this study.

Fig. 7(b) shows a similar dependence of the power density on the anode pressure p_a, i.e., a maximal value of P is achieved at a moderate pressure. The maximum temperature difference, ΔT_{max}, is shown as a function of the current density, I, at different values of anode pressure in Fig. 7(c). With increasing anode pressure p_a, the potential losses first decrease, leading to the decrease in ΔT_{max} since less heat is generated from the losses. Further increase in p_a results in increased losses, which corresponds to the increase in ΔT_{max} at relatively larger p_a. The variation of temperature, however, is observed to be within 0.1 K for the range of p_a. The minimum hydration, λ_{min}, presented in Fig. 7(d) shows a decreasing trend with increasing anode pressure, owing to the reduced water vapor diffusivity. The dehydration of the membrane is apparent at higher anode pressure and current density, and a range of λ_{min} from 14 to 10 is observed in Fig. 7(d).

Since PEM fuel cells operated under conditions of low temperature, high current density and high pressure are prone to membrane dehydration at the anode side, the anode feed stream is always humidified with water vapor. Fig. 8(a)–(d) presents the effect of the relative humidity in the anode feed stream, RH_a, on the performance quantities of the fuel cell. In Fig. 8(a), the cell potential increases monotonically with increasing RH_a, on account of improved hydration and reduced ohmic losses. No apparent improvement in cell potential is observed when RH_a increases from 1.0 to 1.1, which may be explained by the fact that the supersaturated water vapor ($RH_a = 1.1$) will quickly be condensed in the anode electrode, and the actual water vapor concentration in the anode catalyst layer is equivalent to the case of $RH_a = 1.0$. Similarly, the power density increases monotonically with increasing RH_a, as shown in Fig. 8(b). The maximum temperature difference in Fig. 8(c) decreases with increasing anode relative humidity, on account of increased hydration and reduced Joule heating in the membrane region. Relatively small variation of the temperature (<0.2 K) is observed for the wide range of RH_a considered. The minimum hydration, λ_{min}, presented in Fig. 8(d) shows monotonic increase with increasing RH_a, as physically expected. However, no change of λ_{min} is observed with increasing I for a fixed value of RH_a.

It is evident from the parametric effects presented in Figs. 6–8 that increasing the operating temperature can gen-

erally reduce ohmic, transport and activation losses. However, excessive increase in T_c leads to higher water vapor pressure, which, in turn, results in enhanced transport loss. Higher anode pressure may decrease the transport loss, however, membrane dehydration may also occur due to decreased water vapor diffusivity. Using humidified feed stream is favorable to the membrane hydration, while the accompanying water condensation may cause flooding of the electrodes. An optimization of these operating parameters is therefore necessary to determine operating regimes that carefully balance these competing considerations. In this study, the objective of the optimization problem is considered to be that of maximizing the power density, subject to constraints on the maximum temperature difference, the minimum membrane hydration, and the maximum cell potential as explained below. The goal of the optimization problem is to develop the ranges of feasible current density, I, as function of the other operation parameters.

The optimization scheme considered in this study serves as an illustrative example to introduce the methodology for using physics-based models for cell design and optimization. Based on other operational considerations, alternative optimization problems with different objective function and constraints may be solved following the methodology outlined in this study. The roles of the three constraints in deciding the bounds on the operating windows are as follows:

- The consideration of membrane degradation requires that the maximum temperature rise, ΔT_{max}, must be lower than a critical value, ΔT_{crit}. Since ΔT_{max} increases with increasing current density, the constraint on the maximum temperature corresponds to an *upper bound* on the current density. It must be pointed out that the present one-dimensional model can only predict the across-the-cell temperature rise, which is significantly lower than the in-cell temperature rise from the reactant inlet to the outlet. A future work may introduce the in-cell temperature rise constraint by adopting a two- or three-dimensional fuel cell model in the optimization study.
- The membrane hydration is calculated as the ratio of the number of water molecules to the number of charge sites in the membrane, and continuously changes from 0 for a completely dry state to a typical value of 16.8 for a fully hydrated state [10,11]. Since the ionic conductivity of the membrane material increases with increasing membrane hydration, the minimum hydration in the membrane, λ_{min}, must therefore be larger than a lower limit λ_{crit}. Since the membrane hydration decreases with increasing current density, the constraint on the minimum membrane hydration represents a second *upper bound* on the current density. Note that alternatively, the hydration requirement may be posed as an equality constraint on λ_{min} being equal to the fully hydrated value. The results presented in this study, however, are based on the inequality constraint on λ_{min}.
- Since the current density decreases with increasing cell potential, the size and the capital cost of the fuel cell system increase for the higher cell potential. The cell potential must therefore have a upper bound, E_{crit}, determined based on the capital cost consideration. Low cell potential will reduce the efficiency, leading to higher operating cost. Thus, the cell potential must also have a lower bound determined from the efficiency consideration. The cell potential decreases with increasing I, consequently, the constraint on the upper bound of cell potential forms a *lower bound* on the current density. The constraint on the lower bound of cell potential merely provides an additional upper bound on the current density, and is not included in the present optimization scheme for the purpose of conciseness.

The region bounded between the lower bound and the smaller of the two upper bounds on the current density constitutes the operating window for the fuel cell based on the three constraints. The optimum current density variation is one that lies within the operating window and maximizes the power density.

The optimization problem may be written mathematically as

$$\text{Maximize } P \tag{21}$$

subject to:

$$\Delta T_{max} - \Delta T_{crit} \leq 0 \tag{22}$$

$$\lambda_{min} - \lambda_{crit} \geq 0 \tag{23}$$

$$E_{cell} - E_{crit} \leq 0 \tag{24}$$

where the critical values in this study are chosen as: $\Delta T_{crit} = 1.0\,\text{K}$, $\lambda_{crit} = 14$ and $E_{crit} = 0.75\,\text{V}$.

Based on the parametric study shown in Fig. 6, the construction of an example operating window on the current density, I, is illustrated in Fig. 9(a) as a function of the operating temperature, T_c. Corresponding to the constraint on the maximum allowable temperature, shown by the thick straight line in Fig. 6(c), the upper limits of the current density for different values of T_c are indicated by the solid line AB in Fig. 9(a). Similarly, the long-dashed line CD and the chain-dashed line EF in Fig. 9(a) are determined based on the constraints on the minimum membrane hydration and the maximum cell potential, shown in Fig. 6(d) and (a), respectively. The shaded region in Fig. 9(a), enclosed among the three constraints, is identified as the operating window. Values of the current density that lie inside the operating window will ensure that the maximum temperature difference, the minimum membrane hydration and the maximum cell potential are within the prescribed limits that correlate to desired overall cell performance.

While satisfying the specified constraints is a necessary condition, maximizing the power density simultaneously is imperative for affordable fuel cells with small size. The variation of the peak value of the power density with T_c (shown

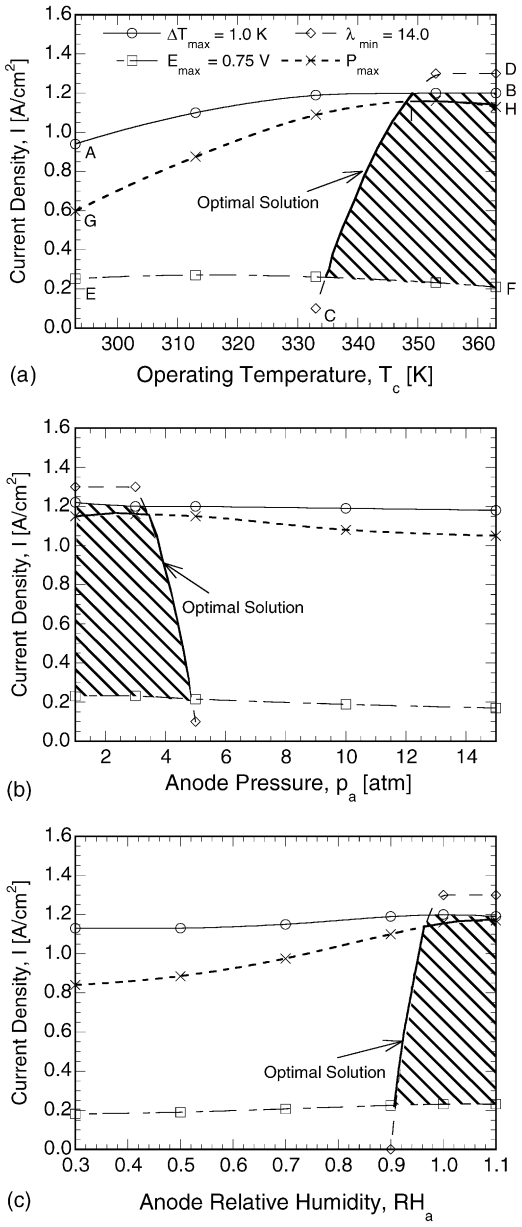

Fig. 9. Operating windows as functions of (a) operating temperature, (b) anode pressure and (c) relative humidity.

by the thick solid curve in Fig. 6(b)) is plotted as the short-dashed line GH in Fig. 9(a). This line represents the unconstrained current density as a function of operating temperature, T_c, required for maximizing the power density. The superposition of the unconstrained solution on the processing window is used to identify the optimal variation of the current density as a function of the operating temperature so as to maximize the power density, P. It is seen in Fig. 9(a) that in the region GI, since the unconstrained current density values for maximizing the power density fall above the upper bound corresponding to the λ_{min} constraint, the upper bound constitutes the constrained optimal solution. In the segment between I and H, the unconstrained optimum current density profile passes within the feasible window, and as a result, satisfies all the specified constraints. The constrained optimum current density variation with the operating temperature is indicated in the plot by the thick solid line. Since the constraints on λ_{min} and E_{max} cannot be satisfied simultaneously when T_c is less than 333 K, neither a feasible operating window nor an optimal solution exist for $T_c < 333$ K. The constrained solution in Fig. 9(a) indicates that operating conditions for fuel cell systems in practice mostly correspond to off-peak values of power density.

Following the foregoing procedure, operating windows and optimal solution of the current density can be obtained for the other operating parameters as well, and the results for the anode pressure and the anode relative humidity are presented in Fig. 9(b) and (c), respectively. In Fig. 9(b), the optimal solution follows the unconstrained optimum current density profile for $p_a < 3.4$ atm. In the interval $3.4\,\text{atm} \leq p_a \leq 5.0\,\text{atm}$, the unconstrained optimum resides above the upper bound corresponding to the λ_{min} constraint, and the upper bound constitutes the constrained optimal solution. When $p_a > 5$ atm, no current density value exists that satisfies both the λ_{min} and E_{max} constraints, which suggests that the fuel cell should not be operated with anode pressure higher than 5.0 atm for the given parameter combination. Corresponding to the decrease in the optimum current density, the power density (not shown in Fig. 9(b)) also decreases significantly with increasing anode pressure, which may be explained by the fact that higher pressure reduces the species diffusivities, leading to larger concentration losses. The decrease in power density at higher anode pressures was also reported by Rowe and Li [13].

In Fig. 9(c), the optimal solution exists when the relative humidity is greater than 0.9. When $RH_a \leq 0.9$, the membrane hydration may become small to violate the λ_{min} constraint, or the cell potential may be high enough to violate the E_{cell} constraint, leading to poor performance of the cell. The results indicate that the anode feed stream needs to be sufficiently hydrated, as physically expected.

The results presented so far pertain to the effects of the operating parameters on the performance of the fuel cell, which are instrumental to the derivation of optimum operating conditions. It is further illustrative to examine the effects of the design parameters to gain insight into the optimum design of the fuel cell, and the corresponding results are presented in Figs. 10–13. Platinum catalyst loading is a critical parameter that governs the available sites for the electrochemical reactions. The dependence of the polarization curve on the cathode platinum loading, $m_{c,pt}$, is illustrated in Fig. 10. When $m_{c,pt}$ increases from 0.32 to 3.00 mg cm^{-2}, the cell potential is observed to have relatively large improvement (about 0.1 V for all the current density values considered), owing to the increased reaction area. Further increase in $m_{c,pt}$ to 8.00 mg cm^{-2} only yields weak increase in the cell potential, indicating that an optimum platinum loading may be determined by simultaneously evaluating the increases in performance and cost. The power density in Fig. 10(b) shows a similar increasing pattern with increasing $m_{c,pt}$, as physically ex-

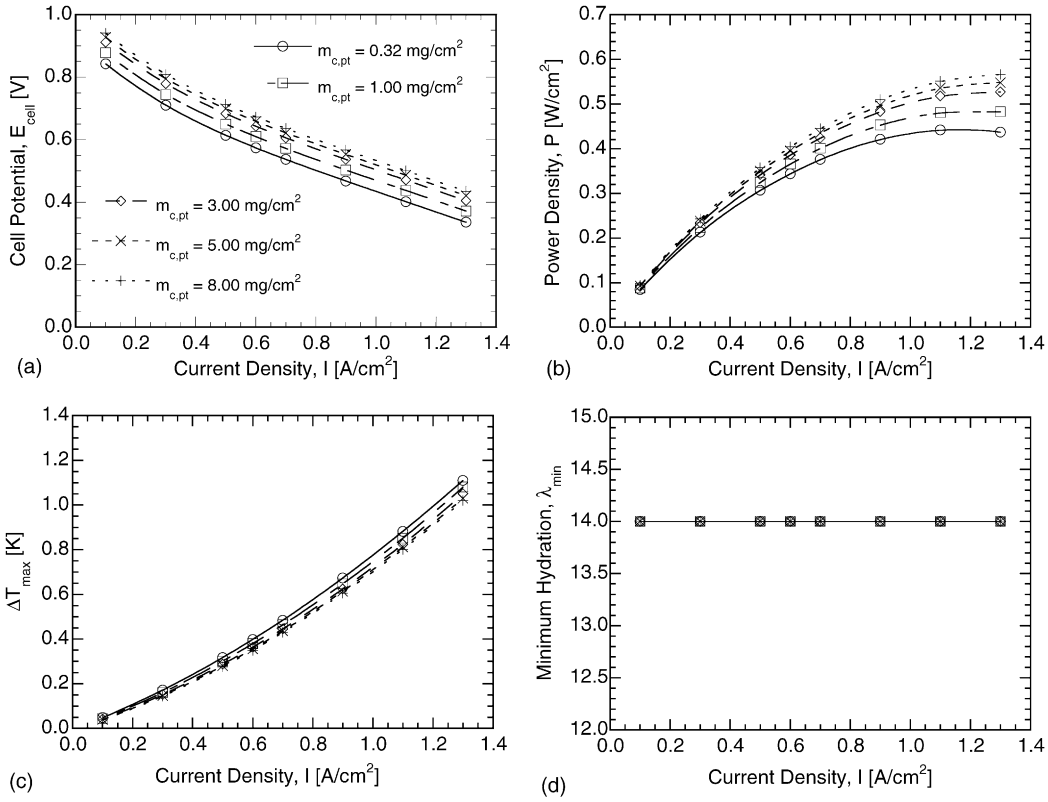

Fig. 10. Parametric effects of I and $m_{c,pt}$ on (a) cell potential, (b) power density, (c) maximum temperature difference and (d) minimum hydration. The default values of the other parameters are given in Tables 1 and 2.

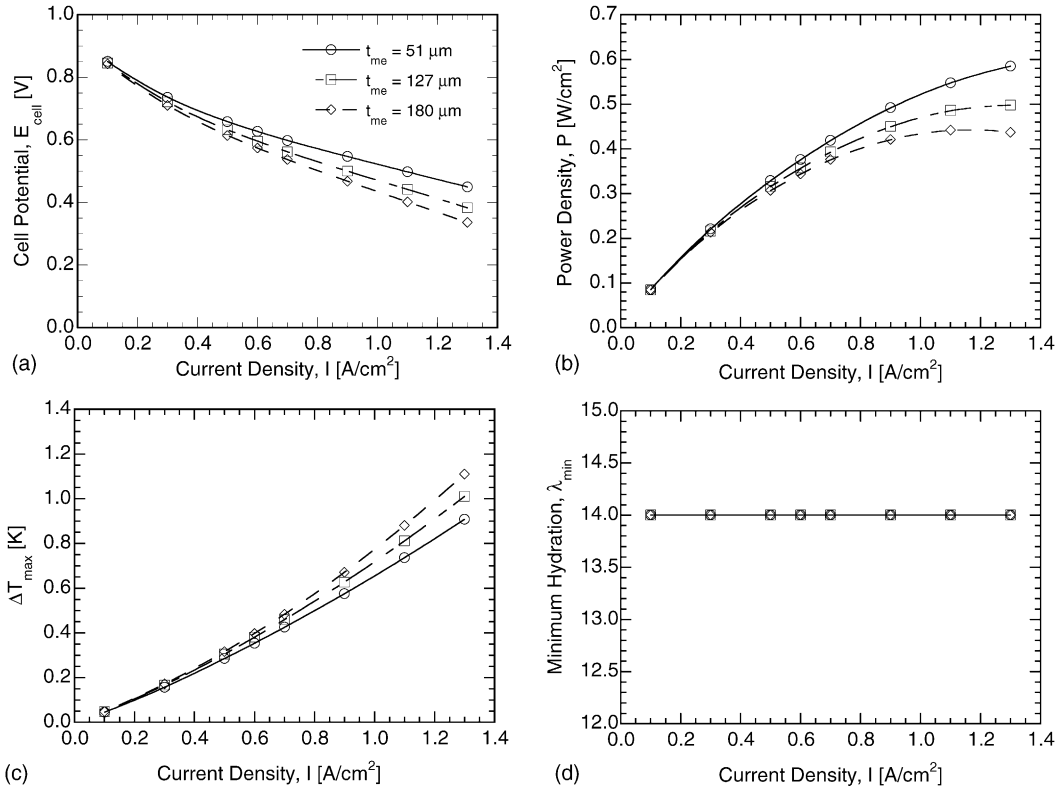

Fig. 11. Parametric effects of I and t_{me} on (a) cell potential, (b) power density, (c) maximum temperature difference and (d) minimum hydration. The default values of the other parameters are given in Tables 1 and 2.

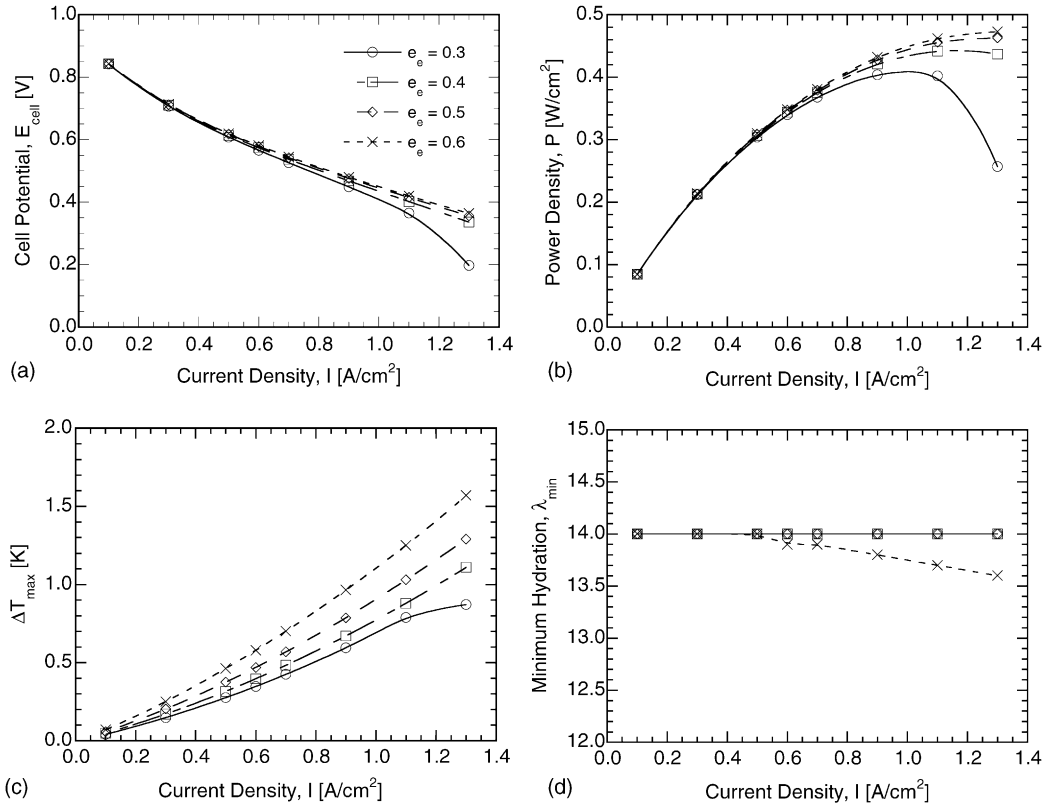

Fig. 12. Parametric effects of I and e_e on (a) cell potential, (b) power density, (c) maximum temperature difference and (d) minimum hydration. The default values of the other parameters are given in Tables 1 and 2.

pected. With increasing platinum loading, the activation loss decreases, leading to monotonic decrease in the maximum temperature difference, as shown in Fig. 10(c). Since the hydration is governed by the water species, $m_{c,pt}$ is observed to have no obvious effect on λ_{min}.

Fig. 11(a)–(d) presents the effect of the membrane thickness, t_{me}, on the four performance quantities. The increase in the membrane thickness results in the decrease in cell potential in Fig. 11(a), owing to the increased membrane resistivity. Similarly, the power density decreases monotonically with increasing t_{me}, as shown in Fig. 11(b). With the increase in t_{me}, the Joule heating in the membrane region increases monotonically, resulting in the increased ΔT_{max} in Fig. 11(c). For the parameter combinations in Fig. 11(d), the minimum hydration, λ_{min}, is observed to be independent of t_{me}. The thicknesses of the electrode and catalyst layers show similar effect as that of t_{me}, and the corresponding results are omitted here for brevity.

The effect of the electrode porosity, e_e, on the polarization curve is shown in Fig. 12(a). Due to smaller mass transport loss at larger electrode porosity, the cell potential is seen to increase monotonically with increasing e_e. For the cases with high current density ($I > 0.9\,A\,cm^{-2}$), the mass transport loss constitutes a large portion of the total loss; thus, the increase in e_e leads to relatively large increase in cell potential, as seen in Fig. 12(a). Similarly, the power density in Fig. 12(b) shows monotonic increase with increasing e_e, and again, larger increases are observed at large values of current density. The maximum temperature difference, ΔT_{max}, increases as the electrode porosity increases, which may be attributed to the increasing Joule heating in the high-porosity electrode region (Fig. 12(c)). The minimum hydration in Fig. 12(d) remains fairly independent of the electrode porosity and the current density. However, for the case $e_e = 0.6$, a slight decrease in λ_{min} is observed with increasing current density, I.

Again, following the procedure in Fig. 9, operating windows and optimal solution of the current density are obtained for the design parameters, $m_{c,pt}$, t_{me} and e_e as depicted in Fig. 13(a)–(c), respectively. In Fig. 13(a), the optimum solution line follows the unconstrained optimum current density profile for $m_{c,pt} < 1.6\,mg\,cm^{-2}$. When $m_{c,pt} \geq 1.6\,mg\,cm^{-2}$, the unconstrained optimum solution exceeds the upper bound corresponding to the ΔT_{max} constraint, and the upper bound denotes the constrained optimal solution. For the entire range of platinum loading considered, the optimum solution of current density exists and only slightly varies between 1.15 and $1.25\,A\,cm^{-2}$. The unconstrained optimal solution line in Fig. 13(b) is observed to be close to the two upper bounds, and the optimum current density has relatively small variation (between 1.15 and $1.30\,A\,cm^{-2}$) with respect to the membrane

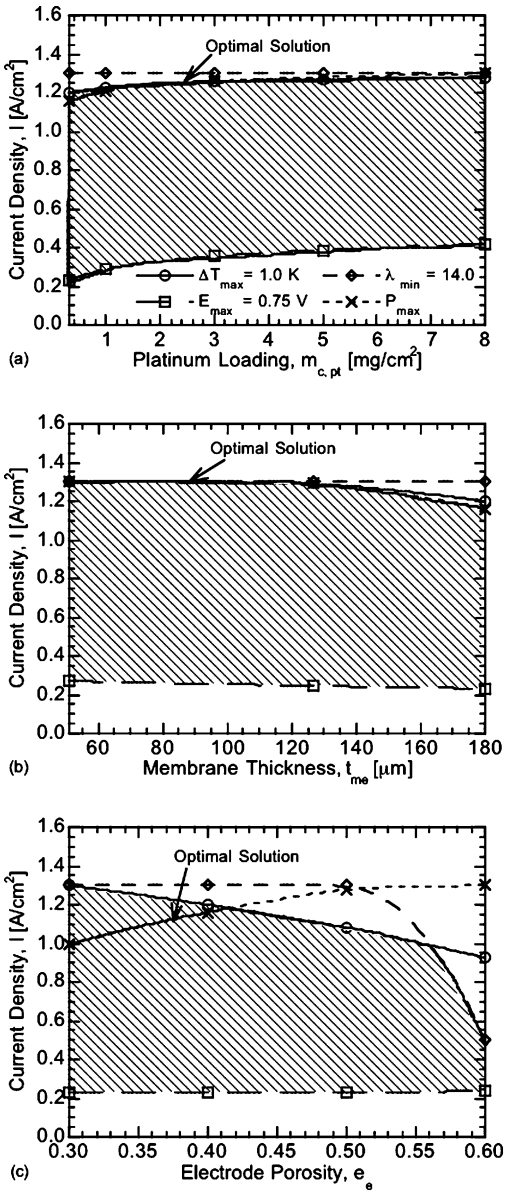

Fig. 13. Operating windows as functions of (a) cathode platinum loading, (b) membrane thickness and (c) electrode porosity.

thickness. However, the optimum power density (not shown in Fig. 13(b)) exhibits significant increase with decreasing membrane thickness (see Fig. 11(b)), which indicates that thinner membrane is preferred in practical applications. The operating window for the electrode porosity is presented in Fig. 13(c), where the optimum solution line follows the unconstrained optimum current density profile as $e_e < 0.415$. The optimum solution is given by the maximum temperature difference constraint in the interval $0.415 \leq e_e \leq 0.562$, and by the minimum hydration constraint when $e_e > 0.562$.

The results in this section provide a comprehensive analysis of a PEM fuel cell operation, and illustrate a methodology for deriving operating envelopes and optimum process designs using physics-based simulation of the cell. Although the operating windows presented are specific to the constraint values chosen, other constraints may be incorporated following the approach outlined. Note that the optimum solutions in Figs. 9 and 13 are obtained by changing one of the operating or design parameters while fixing the values of the remaining ones. These specific solutions determine the values of the current density that maximize the power density for the particular parameter combination chosen for the study. Optimum parameter combinations will be reported in a future work by coupling the present model with numerical optimization procedure [23].

4. Conclusions

A comprehensive one-dimensional steady-state model for a single fuel cell operated with reformate fuel is presented, and a systematic parametric investigation is conducted over a wide range of the fuel cell operating and design conditions. Using the process simulation results, optimum current density is obtained for the first time as a function of various operating and design parameters. For the specific optimization scheme and parameter combinations adopted, it is found that higher operating temperature T_c and anode relative humidity RH_a, and lower anode pressure p_a are required to maximize the power density. The optimum current density does not have significant change with the two design parameters considered in the study, i.e., the platinum loading, $m_{c,pt}$, and the membrane thickness, t_{me}. With the increase in the electrode porosity, the temperature difference and the membrane hydration may become limiting factors to the cell power density. The results provide direct usable information for optimum operating and design of PEM fuel cells. The methodology for determining the operating windows and optimum design configurations may be readily applied to other constraints and cell design specifications.

Acknowledgement

This work was funded by the U.S. Army RDECOM through Contract No. DAAB07-03-3-K-415. The authors gratefully acknowledge the support. The authors also acknowledge the help of Dr. Yonghong Yan in the development of the numerical code used for the study.

References

[1] J. Larminie, A. Dicks, Fuel Cell Systems Explained, Wiley, West Sussex, UK, 2000.
[2] C. Marr, X. Li, An engineering model of proton exchange membrane fuel cell performance, ARI 50 (1998) 190–200.
[3] T.V. Nguyen, R.E. White, A water and heat management model for proton exchange membrane fuel cells, J. Electrochem. Soc. 140 (8) (1993) 2178–2186.

[4] T.F. Fuller, J. Newman, Water and thermal management in solid polymer electrolyte fuel cells, J. Electrochem. Soc. 140 (5) (1993) 1218–1225.
[5] D.M. Bernardi, Water-balance calculations for solid polymer electrolyte fuel cells, J. Electrochem. Soc. 137 (11) (1990) 3344–3351.
[6] T.A. Zawodzinski Jr., T.A. Springer, J. Davey, R. Jestel, C. Lopez, J. Valero, S. Gottesfeld, A comparative study of water uptake and transport through iononomeric fuel cell membranes, J. Electrochem. Soc. 140 (7) (1993) 1981–1985.
[7] T.A. Zawodzinski, C. Derouin, S. Radzinski, R.J. Sherman, V.T. Smith, T.A. Springer, S. Gottesfeld, Water uptake by and transport through Nafion 117 membranes, J. Electrochem. Soc. 140 (4) (1993) 1041–1047.
[8] D.M. Bernardi, M.W. Verbrugge, Mathematical model of a gas diffusion electrode bonded to a polymer electrolyte, AIChE J. 37 (8) (1991) 1151–1163.
[9] D.M. Bernardi, M.W. Verbrugge, A mathematical model of the solid polymer electrolyte fuel cell, J. Electrochem. Soc. 139 (9) (1992) 2477–2745.
[10] T.E. Springer, T.A. Zawodzinski, S. Gottesfeld, Polymer electrolyte fuel cell model, J. Electrochem. Soc. 138 (8) (1991) 2334–2342.
[11] T.E. Springer, M.S. Wilson, S. Gottesfeld, Modeling and experimental diagnostics in polymer electrolyte fuel cells, J. Electrochem. Soc. 140 (12) (1993) 3513–3526.
[12] J.J. Baschuk, X. Li, Modelling of polymer electrolyte membrane fuel cells with variable degrees of water flooding, J. Power Sources 86 (2000) 181–196.
[13] A. Rowe, X. Li, Mathematical modeling of proton exchange membrane fuel cells, J. Power Sources 102 (2001) 82–96.
[14] V. Gurau, H. Liu, S. Kakac, Two-dimensional model for proton exchange membrane fuel cells, AIChE J. 44 (11) (1998) 2410–2422.
[15] S. Um, C.Y. Wang, K.S. Chen, Computational fluid dynamics modeling of proton exchange membrane fuel cells, J. Electrochem. Soc. 147 (2000) 4485–4493.
[16] J.C. Amphlett, R.M. Baumert, R.F. Mann, B.A. Peppley, P.R. Roberge, Performance modeling of the Ballard Mark IV solid polymer electrolyte fuel cell, J. Electrochem. Soc. 142 (1) (1995) 1–15.
[17] J.C. Amphlett, R.F. Mann, B.A. Peppley, P.R. Roberge, A. Rodrigues, A model predicting transient responses of proton exchange membrane fuel cells, J. Power Sources 61 (1996) 183–188.
[18] Z.H. Wang, C.Y. Wang, K.S. Chen, Two-phase flow and transport in the air cathode of proton exchange membrane fuel cells, J. Power Sources 94 (2001) 40–50.
[19] L. You, H. Liu, A two-phase flow and transport model for the cathode of PEM fuel cells, Int. J. Heat Mass Transfer 45 (2002) 2277–2287.
[20] L. You, The two phase flow, transport mechanism and performance studies for PEM fuel cells, Ph.D. dissertation, University of Miami, 2001.
[21] T.E. Springer, T. Rockward, T.A. Zawodzinski, S. Gottesfeld, Model for polymer electrolyte fuel cell operation on reformate feed, J. Electrochem. Soc. 148 (11) (2001) A11–A23.
[22] D. Fan, R.E. White, Modification of Newman's BAND(J) subroutine to multi-region systems containing interior boundaries: MBAND, J. Electrochem. Soc. 138 (6) (1991) 1688-1691.
[23] A. Mawardi, F. Yang, R. Pitchumani, Optimization of the operating parameters of a proton exchange membrane fuel cell for maximum power density, Technical Report TR-04-01, Advanced Materials and Technologies Laboratory, Department of Mechanical Engineering, University of Connecticut, 2004.